

Quantitative phase measurements of human cell nuclei using X-ray ptychography

Jörg Schwenke^{1,2,4*}, Mohammed Yusuf^{1,2,7*}, Laura A. Shemilt^{1,2}, Ulrich Wagner³, Atiqa Sajid⁷, Graeme R. Morrison^{1,2}, Fucui Zhang^{1,2}, Aaron Parsons³, Christoph Rau³, Ian K. Robinson^{1,2,5}

1. London Centre for Nanotechnology, 17-19 Gordon Street, London, WC1H 0AH, United Kingdom
2. Research Complex at Harwell (RCaH), Rutherford Appleton Laboratory, Harwell Oxford, OX11 0FA, United Kingdom
3. Diamond Light Source Ltd, Diamond House, Harwell Science & Innovation Campus, Didcot, OX11 0DE, United Kingdom
4. MAX IV Laboratory, Lund University, P.O. Box 118, SE-22100 Lund, Sweden
5. Condensed Matter Physics and Materials Department, Brookhaven National Lab, Upton NY 11973, USA
6. Division of Biosciences, Department of Life Sciences, College of Health and Life Sciences, Brunel University London, Uxbridge, United Kingdom
7. Centre for Regenerative Medicine and Stem Cell Research, Aga Khan University, Karachi, Pakistan

***Joint first authors and joint corresponding authors**

Corresponding authors details

Dr Mohammed Yusuf, ucanymo@ucl.ac.uk; Mohammed.yusuf@aku.edu

Dr Jorg Schwanke, jorg.schwenke@maxiv.lu.se

Keywords: X-ray, ptychography, nuclei, quantitative phase imaging, synchrotron

Abstract

The human cell nucleus serves as an important organelle holding the genetic blueprint for life. In this work, we applied X-ray ptychography to assess the masses of human cell nuclei, using its unique phase shift information. Measurements were done at the I13-1 beamline at the Diamond Light Source that has extremely large transverse coherence properties. The ptychographic diffractive imaging approach allowed imaging of large structures that gave quantitative measurements of the phase shift in 2D projections. In this paper we present a modified ptychography algorithm that improves the quality of the reconstruction for weak scattering samples. We further demonstrate the application of this approach to calculate the mass of several human nuclei.

Introduction

The cell nucleus is surrounded by the nuclear envelope and separates the chromosomes from the cytoplasm. It is the storage place for genetic information contained in DNA (Pederson, 2011 Alberts *et al.*, 2014). It is also here that important processes of gene expression, replication, recombination and repair, RNA processing and ribosome subunit assembly occur, making the nucleus a defining feature of eukaryotic cells as it determines cell fate (Rippe, 2007, Lamond & Earnshaw, 1998). Alterations of nuclear physical properties have been linked with various diseases (Dahl *et al.*, 2008). In human cells, the nucleus averages 10 μm in diameter in its natural state (Alberts *et al.*, 2014). Its size increases over time until it reaches late prophase (Webster *et al.*, 2009). The nucleus shell is formed by a porous membrane which is filled with nucleoplasm and contains the chromatin (protein-DNA complex) and various other subnuclear bodies at certain points of the cell cycle (Zidovska, 2020). Even though the human nucleus has been studied in great detail, the ‘rich inner life’ is still under investigation (Zidovska, 2020).

Phase-contrast microscopy, that provides quantitative information, can be promising for assessing clinical samples (Wang *et al.*, 2010). In this work, we use coherent x-ray diffraction to image human cell nuclei and extract quantitative information relating to the mass. X-ray diffraction can yield high spatial resolution images in 2D and is suitable for tomography schemes as well (Nishino *et al.*, 2009, Dierolf *et al.*, 2010). The thickness of the sample requires the use of hard x-rays, with

a photon energy above 6 keV to provide the necessary penetration depth. However, due to the reduced absorption, the diffraction efficiency mostly relies on the phase change due to the refractive index in the sample. This makes samples with low electron density (such as biological samples) notoriously difficult to image with hard x-rays, because parasitic scattering from beam line components (e.g. apertures, vacuum windows) can become dominant and appears prominently in the acquired diffraction patterns. These contributions can be greatly reduced by careful beam line design. They can also be eliminated by employing imaging methods that factor out the illumination conditions, such as X-ray ptychography, which we use here.

In ptychography, the sample is scanned in steps smaller than the illumination size and a large number of diffraction patterns is collected (Faulkner *et al.*, 2004, Thibault *et al.*, 2008). Each individual diffraction pattern can be seen as a "view" of the sample, corresponding to a specific area in the two-dimensional sample plan, and containing the diffraction information from this area. It is represented by at least two arrays in the sample plane, one (or more) representing the illumination function, and one (or more) representing the sample view. Because the views overlap, they contain redundant information and by assuming that the illumination is constant (or varying slowly), the diffraction contribution from the sample can be isolated and a complex real-space image of the sample can be reconstructed through iterative phase retrieval. In practice, numerical phase retrieval can still be difficult when the diffracted intensity is close to the noise level, as it is with the samples in this work. Standard implementations of the common numerical algorithms do not yield satisfactory convergence in every case, but stagnate without producing a unique solution that is in agreement with the diffraction data (Dierolf *et al.*, 2010). Over the past years, many improvements to the algorithms have been suggested that improve the convergence of the algorithm or use constraints to remove artefacts (e.g.: Thibault *et al.*, 2012, Huang *et al.*, 2014, Maiden *et al.*, 2017). We have found that one particular refinement of the algorithm, reciprocal space sub-sampling, first suggested by Batey *et al.*, leads to significant improvement in the phase retrieval of weakly scattering samples (Batey *et al.*, 2014).

In this article, we describe the implementation of a refined ptychography algorithm and its application to human nuclei. We also discuss the use of the retrieved phase information to quantify the mass distribution of the sample, based on assumptions of the molecular composition.

Material and Methods

Cell culture and nuclei preparation

Cells were grown according to previously published protocols (Yusuf *et al.*, 2014a, b). A B-lymphocyte male Yoruba cell line (passage 4); (GM18507) was cultured at 37°C in a 5% CO₂ atmosphere using RPMI medium supplemented with 100 U/ml penicillin and 100 µg/ml streptomycin (Gibco), 20% FBS (reagents purchased from Sigma-Aldrich, Dorset, UK) and 1% L-glutamine (Sigma Aldrich, UK). Cells were arrested in metaphase after treatment with Colcemid (0.2 µg/ml, Gibco BRL); (0.2 µg/mL (Gibco Life Technologies, Paisley, UK) overnight followed by KCL (0.075 M); (VWR BDH Prolabo, Dublin, Ireland) treatment at 37°C for 5 min. Nuclei were extracted and fixed in carnoy's solution (3:1 methanol/acetic acid) and 0.5% glutaraldehyde (Sigma) (10 mM Hepes-KOH and 5 mM MgCl₂) according to Shemilt *et al.* (2015). The sample material was placed onto 100 nm thick silicon nitride windows (Silson, UK) and stained with 150 µM Syber gold dye. The sample was washed using water and then left to air dry. The samples were imaged using a Zeiss AxioZ2 microscope with Isis software (Metasystems) to provide both visible and fluorescence images for reference and correlation. Overall 3 samples, numbered 1, 2 and 3, were used in the study samples 1 and 2 were stained with platinum blue (Wanner *et al.*, 1995; Yusuf *et al.*, 2014a) at 5 mM concentration for 30 minutes and washed in water.

X-ray ptychography data acquisition

The experiments were carried out at the I13-1 coherence beamline at the Diamond Light Source in Harwell, UK (Pešić *et al.*, 2013). For this experiment a photon energy of 7.5 keV was used and the X-ray beam was collimated by a compound refractive lens at the front end. I13-1 is specifically designed to maximize transverse coherence: it consists of a 250 m section between front end and the monochromator which allows for a transverse coherence length exceeding 200 µm in the vertical direction (Rau *et al.*, 2011). After the monochromator, the beam was cropped by a pinhole aperture of diameter $D = 20$ µm, so that the x-ray probe on the sample plane is larger than the expected size of a human nucleus. The sample was mounted on a stack of piezo-electric translation stages in a vacuum environment at a pressure of about 10 mbar during the measurements, without

active pumping. There were no vacuum windows between the pinhole aperture and the far end of the flight tube, where a Kapton window was installed directly in front of the detector, a MEDIPix2 (de Vries *et al.*, 2007), a discrete pixel-array detector with pixel size $p = 55 \mu\text{m}$. The distance between the sample and the detector was about $L = 15 \text{ m}$, and the array size is cropped to 450×450 pixels, which gives a corresponding real space pixel size of 200 nm at 7.5 keV . A partially-transparent beamstop, made of Tungsten with a thickness of $10 \mu\text{m}$ was glued to a separate Kapton foil and placed in front of the detector to attenuate the zero-order beam. A schematic diagram of the imaging setup is shown in Figure 1. Figure 2 shows a typical diffraction pattern acquired from the measurements. Typical scan parameters were 5 seconds exposure time per diffraction pattern, and average step size of $2 \mu\text{m}$ between scan positions, which were distributed to fill a circle using Poisson Disk sampling (Dunbar *et al.*, 2006) and sorted into a spiral scan path trajectory.

Phase retrieval algorithm

Ptychography is an iterative phase retrieval scheme that aims to find the correct complex phase for each pixel of a set of measured diffraction patterns, where only the intensities are recorded. A full description of the algorithm can be found in Maiden *et al.*, 2009. Here we will focus on the sampling aspect and the reciprocal space sampling, which is based on the physical pixel size of the detector and the experimental geometry. The recorded intensities in the reciprocal plane are the square modulus of the far-field diffraction patterns. The recorded intensity $I_j(\mathbf{u})$ at reciprocal-space coordinate \mathbf{u} of diffraction pattern j can be calculated from the probe function P and the object function O as:

$$(1) \quad I_j(\mathbf{u}) = |\mathcal{F}[O(\mathbf{r})P(\mathbf{r} - \mathbf{R}_j)]|^2$$

where \mathcal{F} is the two-dimensional Fourier transform, \mathbf{r} is a coordinate vector in sample space and \mathbf{R}_j is the movement of the probe relative to the object for the j -th measurement. The Product $O(\mathbf{r})P(\mathbf{r} - \mathbf{R}_j)$ forms the exit wave $\psi_j(\mathbf{r})$ for that particular view.

According to Edo *et al.*, 2013, the experimental geometry must be set such that the smallest interference fringes can be sampled by the detector:

$$(2) \quad \frac{L\lambda}{Dp} > 2.$$

The linear oversampling ratio S_o describes by how much the minimum requirement is exceeded in any given experimental geometry:

$$(3) \quad S_o = \frac{L \lambda}{2 p} \frac{1}{D}.$$

Values of S_o larger than one are theoretically sufficient for phase retrieval but often require *a-priori* knowledge of either the illumination or the sample. It has been shown recently (Edo *et al.*, 2013) that ptychography can be used even in under-sampled conditions $S_o < 1$, as the overlap redundancy in real space compensates for the under-sampling in diffraction space. Edo *et al.* showed that the step size by which the illumination is shifted between exposures is a crucial parameter in ptychography, and they provide a useful figure of merit that we will refer to as the ptychography sampling ratio S_p , where

$$(4) \quad S_p = \frac{L \lambda}{2 p} \frac{1}{R}.$$

Here R denotes the average step-size in between exposures. This measure replaces the pinhole size D from the linear oversampling ratio, as the aperture size is irrelevant in ptychography. In this formulation, sampling ratios S_p larger than 1 are considered sufficient for successful reconstruction. The step-size R can be adjusted to compensate for either a large pixel size p or a short detector distance L , thus allowing for geometries with large detector acceptance angle capable of producing reconstructions with high spatial resolution.

In our experimental geometry, the linear oversampling criterion was just met: $S_o = 1.2$. This is due to the large diameter of the pinhole, which was chosen to exploit the excellent transverse coherence of the beam and increase the total x-ray flux. However, our setup reaches values of S_p between 10 and 30, depending on the scan pattern used. Under these conditions, we found that ptychography scans of strongly scattering samples, such as a test sample made of tungsten, could be reconstructed without any *a priori* knowledge of the illumination function.

We here employ a reciprocal space up-sampling algorithm as suggested by Batey *et al.*, in which the pixels in the diffraction patterns are split into sub-pixels to simulate a detector with smaller physical detector pitch than actually used (Batey *et al.*, 2014). The method can be used to reconstruct diffraction data that nominally violates the ptychography sampling condition, but they also report a general improvement in the quality of the reconstruction. They note that even in cases

that fulfil the sampling condition, the quality of the reconstruction can be improved. We use this method to obtain good reconstructions of our weakly scattering data:

We use N to denote the number of pixels that take up one physical space along each dimension, so that each pixel is replaced by N^2 subpixels. Due to the properties of the Fourier transform, a finer pixel pitch in reciprocal space results in a larger field of view in real space. For the iterative phase retrieval, the real-space arrays for the illumination function and the initial guess for each view are therefore padded with zeros on all sides to increase the array size by a factor of N^2 . The exit wave is propagated by Fourier transformation to the detector plane, where each physical detector pixel m is now represented by N^2 virtual pixels labelled n . In the detector plane the modulus constraint is applied by comparing the measured pixel intensity I_m with the virtual sub-pixels. Each artificial pixel $\Psi'_{j,m,n}$ is updated according to:

$$(5) \quad \Psi'_{j,m,n} = \Psi_{j,m,n} \frac{\sqrt{I_m}}{\sqrt{\sum_{n=1}^{N^2} |\Psi_{j,m,n}|^2}}_{j,m,n}$$

In simple terms, the squared sum of the artificial sub-pixels is made to agree with the measured intensity I_m for the corresponding real pixel, by a normalization coefficient, and multiplying the coefficient with each sub-pixel, thus preserving the ratio between sub-pixels values. The modified function $\Psi'_{j,m,n}$ is then propagated back to the object plane by inverse Fourier transform to determine the updated exit wave $\psi'_j(\mathbf{r})$ in the object plane. As was seen before, the use of sub-sampling results in an expanded object function in the real space. However, the data in this region is unconstrained and deteriorates into numerical noise.

Quantitative analysis

The phase shift ϕ is reconstructed quantitatively in units of the wavenumber of the illumination as a projection in the direction of x-ray propagation. The quantitative phase shift can be directly converted into a spatial map of the projected electron density, σ_e , based on the classical electron radius r_0 (Giewekemeyer *et al.*, 2009).

$$(6) \quad \sigma_e = -\frac{\phi}{\lambda r_0}$$

The electron density can be therefore used to estimate the mass thickness of the imaged features using an averaged atomic mass number A , an average atomic number Z , and the atomic mass unit u :

$$(7) \quad \sigma_m = \frac{Au}{Z} \sigma_e.$$

For human cell nuclei, which mostly consist of light elements (CHNO), the ratio A/Z is very close to two. We can integrate the mass density of nuclei identified in the reconstructions and estimate the total mass.

Results

The samples containing cell nuclei, are composed of mostly low- Z elements, which are almost transparent to hard X-rays and only cause small phase changes in the illumination wave front. The diffraction patterns collected from these samples are consequently dominated by diffraction at the pinhole aperture that was used to define the beam, as shown in figure 2.

A clear image of the sample could not be reconstructed from these datasets, even with detailed knowledge of the illumination obtained from reconstructions of the test samples. Figure 3 shows a reconstruction made using a the standard algorithm described in Maiden *et al.*, 2009, while Figure 4 shows a reconstruction made with the modified algorithm using sub-pixels (2×2). The figures show both the reconstructed complex probe array as a HSV plot, and the reconstructed phase shift of the object. The reconstruction using sub-pixels is significantly better in both parts, the probe function in particular is a far better representation of the pinhole. The sample function is also more detailed and less blurry.

One way to assess the performance of the phase retrieval is the use of an error function in the reciprocal plane, where the current iterate is compared with the measured data:

$$(8) \quad Err = \sum_j \frac{\sum_m |\sqrt{I_m} - |\Psi_m||^2}{\sum_m |\sqrt{I_m}|^2}.$$

Here I_m is the intensity measured in pixel m of diffraction pattern j , while Ψ_m is the retrieved complex value for the same pixel. The virtual sub-pixels are summed before the error is calculated. Figure 5 shows the error functions for the two reconstructions in figures 3 and 4. The error can be

reduced by almost two orders of magnitude by sub-sampling the data during the reconstruction process. Figure 6 shows a comparison between the measured data (a) and the final iterate (b), the exit wave corresponding to the same diffraction pattern as in figures 2 and 6a). The area shown is cropped from the full array, illustrated by the white rectangle in figure 2. As can be seen, the pixel size is smaller in figure 6b), due to the use of sub-pixels. The algorithm has filled in the missing data from the measurement with data from other diffraction patterns.

Figure 7 shows the Fourier ring correlation function (FRC) for the stained nucleus sample 1 shown in figures 3 and 4. The FRC indicates the information validity of the reconstruction by comparing two reconstructions of the same object. The abscissa shows full spatial period of the frequency components in the diffraction data. The data cuts off at about 400 nm (200 nm half-period) due to the size of the detector array (see above). The FRC-function is compared to the 3σ -threshold (Van Heel *et al.*, 2005), and is above the threshold and therefore valid over the spatial frequency interval observed. Based on the sampling conditions and the visible features, we find the resolution to be 200 nm, the physical pixel size in the sample plane, and one half-period of the largest diffracted frequency measured by the detector.

A total of 13 datasets were used for the quantitative analysis. For each dataset, the phase retrieval was repeated 30 times with different random seeds and the reconstructed phase shift was averaged. A histogram of the pixel phase values was used to determine the phase offset for the membrane surrounding the nuclei. The nuclei were isolated from the background by setting a threshold at three standard deviations above the normal distribution peak of membrane background. In cases where nuclei were not completely isolated, watershed segmentation was applied using the MATLAB in-built function to define the nucleus (MATLAB). Figure 7 shows segmented nuclei A and B as identified in figure 4a).

The recovered phase properties of the nuclei were then used according to equations (6) and (7) to calculate the integrated mass. The area was determined by counting the number of pixels that each nucleus occupies above the threshold. Table 1 shows a comparison of the average mass, area, and mass density for the three samples, while figure 9 shows a histogram of all the nuclei examined (Samples 1 (blue) and 2 (yellow) are stained with platinum blue and Sample 3 (red), unstained).

	Mass (pg)	Area (μm^2)	Mass density (pg/μm^2)
Sample 1	75.1 \pm 50.6	26.4 \pm 10.3	2.7 \pm 1.0
Sample 2	91.1 \pm 90.0	25.9 \pm 11.6	3.0 \pm 1.7
Sample 3	49.7 \pm 23.7	58.5 \pm 15.5	0.84 \pm 0.32

Table 1: Average mass, area, and mass density for the three samples.

Overall a varied range of masses were observed from all the samples. Sample 1 and 2 displayed a cluster approximately between 30 to 80 pg. Sample 1 had 2 nuclei with a high mass of 140 and 190 pg. Sample 3 showed a cluster approximately around 50 pg with the 2 nuclei displaying a mass above 80 pg.

Finally, figure 10 shows the relationship between the occupied area of the nuclei and their respective mass. A linear regression is also plotted for each sample. The plot shows a linear relationship between the area and mass. Samples 1 (blue) and 2 (yellow) are stained with platinum blue and Sample 3 (red), unstained. The 3 samples showed differences in the occupied area for nuclei measured. For each sample an increase in mass was observed with increase in occupied area.

Discussion

In this study, X-ray ptychography was performed on human cell nuclei giving quantitative measurements of the phase allowing a direct estimation of the mass. We find that ptychography is suitable for routine imaging of weak phase objects such as organic tissue illuminated with hard X-ray radiation. The application of reciprocal space up-sampling during the iterative phase retrieval was crucial in the presented study and could potentially become a standard modification when dealing with weak phase materials.

As shown in Figure 3, the Error was significantly reduced in this way as the reconstructed image appears to be more detailed, as shown in Figure 2. The method does not affect the theoretical resolution of the reconstructed image because the up-sampling in the detector plane transfers to an extended object and illumination functions in real space. However, in practice, the reconstruction matches much more closely the true values of the sample and therefore smaller features of the sample become visible.

The obtained nuclei masses of the unstained samples were around 40 pg. Compared to unstained, Pt-stained samples showed a varied range of masses between 30 to 80 pg. No major changes in the mass between unstained and stained samples was seen except for 2 nuclei that displayed a mass above 80 pg which may be due to additional Pt residue during sample preparation. Other studies have also observed a wide range of masses after performing quantitative electron microscopy on human interphase nuclei from blood lymphocytes (Golomb & Bahr, 1974). Overall a bimodal distribution was seen with a mass range of 65 pg and 88 pg (Golomb and Bahr, 1974) that is in close agreement with the findings of this study. Other studies have determined the mass of human nuclei ranging in the lower end 45 pg -55pg (Sandritter *et al.*, 1963; Sandritter & Muller, 1959) and high end 71.93 -83.59 pg (Bahr and Golomb, 1971).

A possible reason for variation seen in our study is that the sample might have been at different stages of the cell cycle. As the nucleus resides inside the cell throughout interphase (G₁, S, and G₂), it reaches prophase where the nuclear envelope breaks down that is then rebuilt back at telophase. As a cell progresses through the cell cycle, the size of the nucleus monotonously increases over hours and undergoes various reorganization including its size and DNA/protein content (Chu *et al.*, 2017). As there is a broad range of determined nucleus masses found in our data, we can divide our population sampled into two different states between 30 and 50 pg and between 65 and 90 pg, indicating that they may be in G₁ to early S and late S to G₂-M, respectively. This differentiation can be interpreted as due to cells in metaphase (after DNA replication) and interphase (before DNA replication).

The DNA content of a nucleus in G₁ is diploid (2N), early S phase is 2N and late S phase is 4N, tetraploid in G₂ through to M (4N) (Yang, 2018). The expected DNA mass for the full haploid human genome (3.5x10⁹ base pairs of DNA) is 3.5 pg for a single strand of double helix, plus 5 pg of protein in the known histones with one octamer per 170 base pairs (Woodcock *et al.*, 1984). Known non-histone proteins account for 50% more, or 2.5 pg (Uchiyama *et al.*, 2005). The tetraploid genome per nucleus having 4 copies adds up to 44 pg that would be 22 pg in early interphase having 2 copies. Apart from chromatin and non-histone proteins the nucleus consists of the nucleoplasm with subnuclear bodies that include the nucleoli, cajal bodies, PML bodies, speckles and nuclear membrane (Misteli & Spector 2011; Chu *et al.*, 2017) whose mass should also be taken into account.

The size (area) of stained (platinum stained) and no platinum stained nuclei from the ptychographic images showed variation indicating a different degree of spreading out on the membrane. Yet the range of masses seen is about the same for all the samples except 2 nuclei from sample 1 (platinum stained). This is supported by studies showing an increase of nuclear volume (besides increase in mass) in metaphase (Umen *et al.*, 2005). Unfortunately, the two-dimensional projections do not directly relate to the volume of the nuclei. The mass should in principle be better correlated with the different stages of the cell cycle.

We suggest that the measurement method used in this study is sensitive enough to distinguish between different cell cycle states between which the DNA and histone in the nucleus differs by a factor of two. In the future a controlled study investigating nuclei at various cell cycle states (with synchronization at different stages) is needed with the described approach. The efficiency of the method could be significantly improved by refocusing the x-ray beam with reflective optics, and by employing on-the-fly scanning techniques to reduce motion control overhead (Clark *et al.*, 2014). Overall X-ray ptychography could serve useful for measuring nuclear masses in different cell types (normal and diseased) giving subcellular characteristics and assist in medical diagnosis as well as for biological research.

Conclusion

In this study, we investigated the application of ptychography for quantitative phase imaging of human cell nuclei. This approach is promising as the ptychographic reconstructions of the nuclei were much improved using the up-sampling technique, which is very successful when dealing with weakly scattering objects. The retrieved phase measurements of human nuclei show a wide distribution of nucleus mass that cannot be easily reconciled with theoretical estimates. The results show that the mass varies considerably. This can be explained by different aggregation phases of the nuclei, or variations in the binding of the Pt stain. A more robust study would both require a better understanding of the binding efficiency of the Pt stain and a larger sample size.

Acknowledgements

We acknowledge funding in the Research Complex at Harwell from a BBSRC Professorial Fellowship ‘Diamond Professorial Fellowship for imaging chromosomes by coherent X-ray

diffraction'. Work at Brookhaven National Laboratory was supported by the US Department of Energy, Office of Science, Office of Basic Energy Sciences, under Contract No. DE-SC0012704. Financial support was also provided by Professor El-Nasir Lalani at the Aga Khan University and generous donors.

References

Alberts, B., Johnson, A., Lewis, J., Morgan, D., Raff, M., Roberts, K., & Walter, P. (2014). *Molecular Biology of the Cell* 6th ed (New York, NY: Garland Science).

Bahr, G. F., & Golomb, H. M. (1971). Karyotyping of single human chromosomes from dry mass determined by electron microscopy. *Proceedings of the National Academy of Sciences*, 68(4), 726-730.

Batey, D. J., Edo, T. B., Rau, C., Wagner, U., Pešić, Z. D., Waigh, T. A. & Rodenburg, J. M. (2014). *Phys. Rev. A* 89, 043812.

Clark, J. N., Huang, X., Harder, R. J., & Robinson, I. K. (2014). Continuous scanning mode for ptychography. *Optics letters*, 39(20), 6066-6069.

Chu, F. Y., Haley, S. C., & Zidovska, A. (2017). On the origin of shape fluctuations of the cell nucleus. *Proceedings of the National Academy of Sciences*, 114(39), 10338-10343.

Dahl, K. N., Ribeiro, A. J., & Lammerding, J. (2008). Nuclear shape, mechanics, and mechanotransduction. *Circulation research*, 102(11), 1307-1318.

De Vries, R. I., Weijers, S., Bethke, K., Kogan, V., Vasterink, J., Kharchenko, A., Fransen, M. & Bethke, J. (2007). *Nucl. Instrum. Meth. A*. 576(1), 164-168.

Dierolf, M., Menzel, A., Thibault, P., Schneider, P., Kewish, C. M., Wepf, R., Bunk, O. & Pfeiffer, F. (2010). *Nature* 467, 436-439.

Dierolf, M., Thibault, P., Menzel, A., Kewish, C.M., Jefimovs, K., Schlichting, I., von König, K., Bunk, O. & Pfeiffer, F. (2010). *New J. Phys.* 12

Dunbar, D., & Humphreys, G. (2006). A spatial data structure for fast Poisson-disk sample generation. *ACM Transactions on Graphics (TOG)*, 25(3), 503-508.

Edo, T. B., Batey, D. J., Maiden, A. M., Rau, C., Wagner, U., Pešić, Z. D., Waigh, T. A. & Rodenburg, J. M. (2013). *Phys. Rev. A* 87, 053850.

Faulkner, H. M. L., & Rodenburg, J. M. (2004). Movable aperture lensless transmission microscopy: a novel phase retrieval algorithm. *Physical review letters*, 93(2), 023903.

Giewekemeyer, K., Thibault, P., Kalbfleisch, S., Beerlink, A., Kewish, C. M., Dierolf, M., Pfeiffer, F. & Salditt, T. (2009). *P. Natl. Acad. Sci. USA*. 107, 529-534.

Golomb, H. M., & Bahr, G. F. (1974). Electron microscopy of human interphase nuclei. *Chromosoma*, 46(3), 233-245.

Huang, X., Yan, H., Harder, R., Hwu, Y., Robinson, I. K., & Chu, Y. S. (2014). Optimization of overlap uniformness for ptychography. *Optics Express*, 22(10), 12634-12644.

Lamond, A. I., & Earnshaw, W. C. (1998). Structure and function in the nucleus. *Science (New York, N.Y.)*, 280(5363), 547-553.

Maiden, A. M., & Rodenburg, J. M. (2009). An improved ptychographical phase retrieval algorithm for diffractive imaging. *Ultramicroscopy*, 109(10), 1256-1262.

Maiden, A., Johnson, D., & Li, P. (2017). Further improvements to the ptychographical iterative engine. *Optica*, 4(7), 736-745.

Misteli T, Spector DL (2011) The nucleus. vol 3, no 2. Cold Spring Harbor Laboratory Press, New York

Nishino, Y., Takahashi, Y., Imamoto, N., Ishikawa, T. & Maeshima, K. (2009). *Phys. Rev. Lett.* 102(1), 018101.

Pederson, T. (2011). The nucleus introduced. *Cold Spring Harbor perspectives in biology*, 3(5), a000521.

Pešić, Z. D., De Fanis, A., Wagner, U., & Rau, C. (2013, March). Experimental stations at I13 beamline at Diamond Light Source. In *Journal of Physics: Conference Series* (Vol. 425, No. 18, p. 182003). IOP Publishing.

Rau, C., Wagner, U., Pešić, Z., & De Fanis, A. (2011). Coherent imaging at the Diamond beamline I13. *physica status solidi (a)*, 208(11), 2522-2525.

Rippe, K. (2007). Dynamic organization of the cell nucleus. *Current opinion in genetics & development*, 17(5), 373-380.

Sandritter, W., and D. Müller. "Vergleichende röntgenhistoradiographische und interferenzmikroskopische Trockengewichts-bestimmungen." *Experientia* 15, no. 4 (1959): 158-159.

Sandritter, W., Zilles, H., & Kiefer, G. (1963). Interference microscopic dry weight determinations on cells from the vaginal epithelium. *Acta cytologica*, 7, 45-53.

Shemilt, L., Verbanis, E., Schwenke, J., Estandarte, A. K., Xiong, G., Harder, R., Parmar, N., Yusuf, M., Zhang, F. & Robinson, I. K. (2015) *Biophys J.* 108(3), 706–713.

Thibault, P., Dierolf, M., Menzel, A., Bunk, O., David, C., & Pfeiffer, F. (2008). High-resolution scanning x-ray diffraction microscopy. *Science*, 321(5887), 379-382.

Thibault, P., & Guizar-Sicairos, M. (2012). Maximum-likelihood refinement for coherent diffractive imaging. *New Journal of Physics*, 14(6), 063004.

Uchiyama, S., Kobayashi, S., Takata, H., Ishihara, T., Hori, N., Higashi, T., ... & Fukui, K. (2005). Proteome analysis of human metaphase chromosomes. *Journal of Biological Chemistry*, 280(17), 16994-17004.

Umen, J. G. (2005). The elusive sizer. *Current opinion in cell biology*, 17(4), 435-441.

Van Heel, M., & Schatz, M. (2005). Fourier shell correlation threshold criteria. *Journal of structural biology*, 151(3), 250-262.

Wang, P., Bista, R., Bhargava, R., Brand, R. E., & Liu, Y. (2010). Spatial-domain low-coherence quantitative phase microscopy for cancer diagnosis. *Optics letters*, 35(17), 2840-2842.

Wanner, G., & Formanek, H. (1995). Imaging of DNA in human and plant chromosomes by high-resolution scanning electron microscopy. *Chromosome Research*, 3(6), 368-374.

Webster, M., Witkin, K. L., & Cohen-Fix, O. (2009). Sizing up the nucleus: nuclear shape, size and nuclear-envelope assembly. *Journal of cell science*, 122(10), 1477-1486.

Woodcock, C. L. F., & Frank, J. (1984). Nucleosome mass distribution using image averaging. *Journal of ultrastructure research*, 89(3), 295-302.

Yang, V. W. (2018). The cell cycle. *Physiology of the Gastrointestinal Tract*, 197-219.

Yusuf, M., Parmar, N., Bhella, G. K., & Robinson, I. K. (2014). A simple filtration technique for obtaining purified human chromosomes in suspension. *Biotechniques*, 56(5), 257-261a.

Yusuf, M., Chen, B., Hashimoto, T., Estandarte, A. K., Thompson, G., & Robinson, I. (2014). Staining and embedding of human chromosomes for 3-D serial block-face scanning electron microscopy. *Biotechniques*, 57(6), 302-307b.

Zidovska A. (2020). The rich inner life of the cell nucleus: dynamic organization, active flows, and emergent rheology. *Biophysical reviews*, 12(5), 1093–1106.

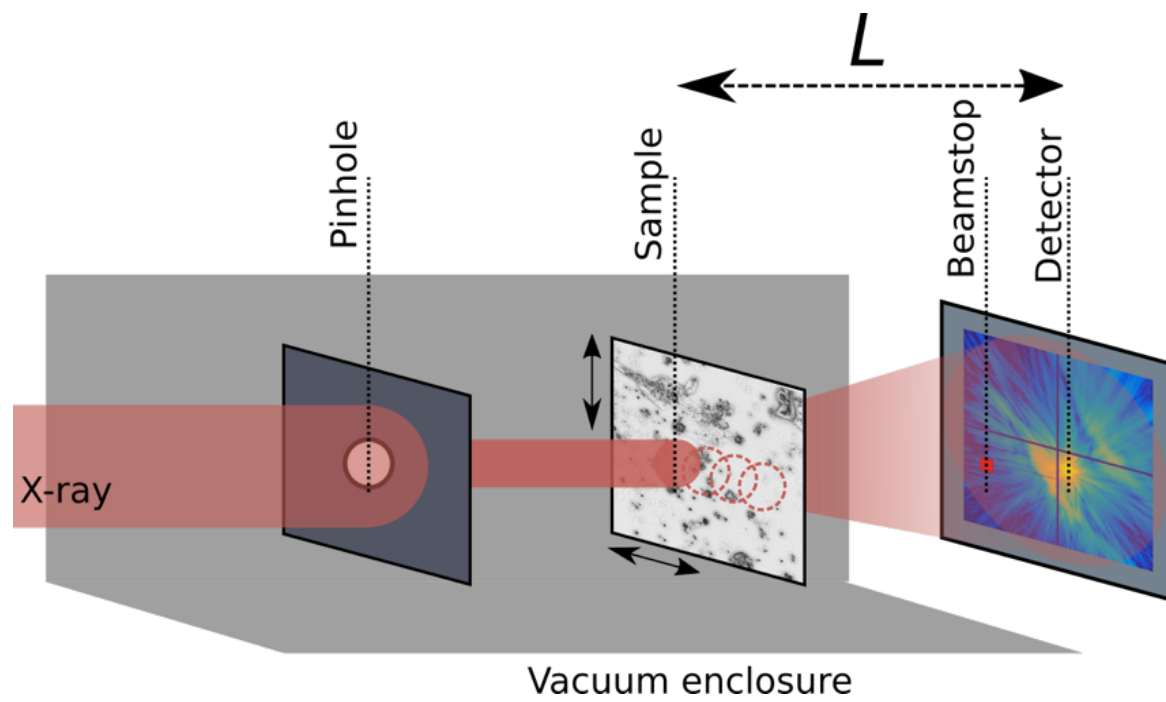


Figure 1. Experimental imaging setup at Diamond Light Source I13-1.

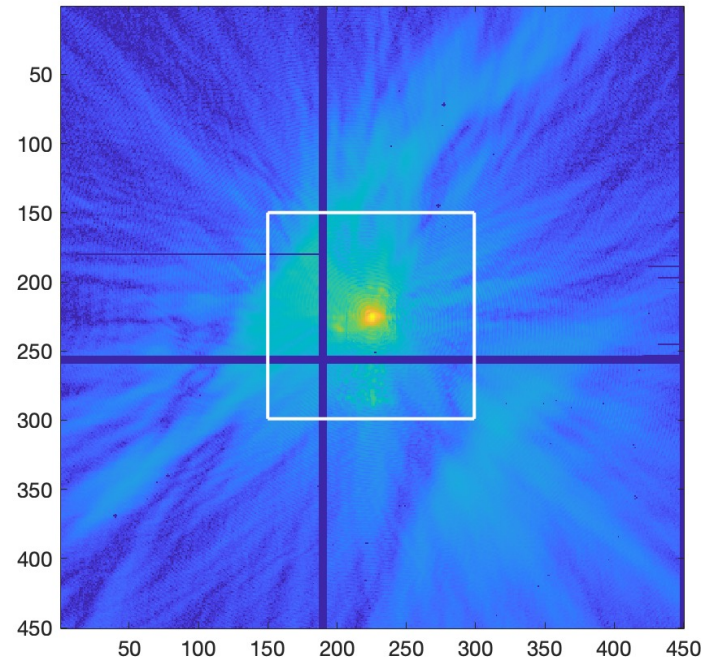


Figure 2: Full detector frame from a nuclei dataset (log plot). The zero order is centered. The dark blue lines represent missing data due to gaps between the detector areas and dead pixels. The white square marks the cropped area shown in Fig Y.

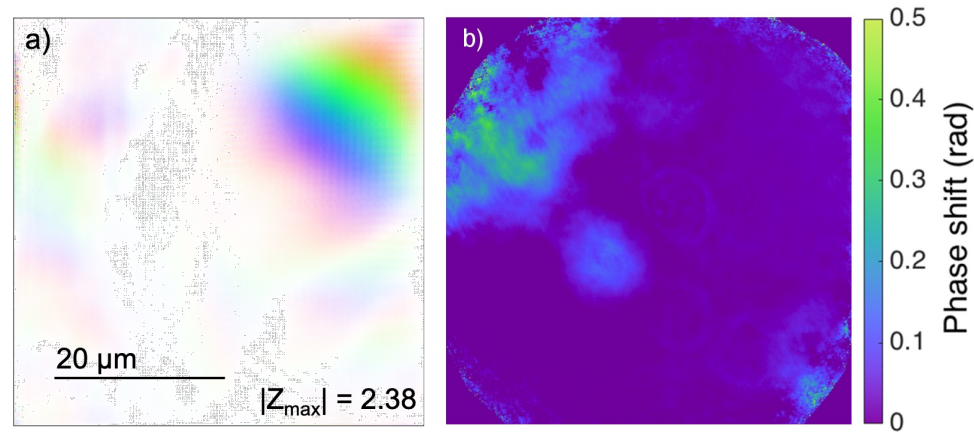


Figure 3: Reconstruction of a dataset using actual pixel size. The probe function (a), HSV plot, see R2a) for legend) is not recovered properly, but off-center and distributed over the entire array. The reconstructed phase (b), phase plot) is blurry.

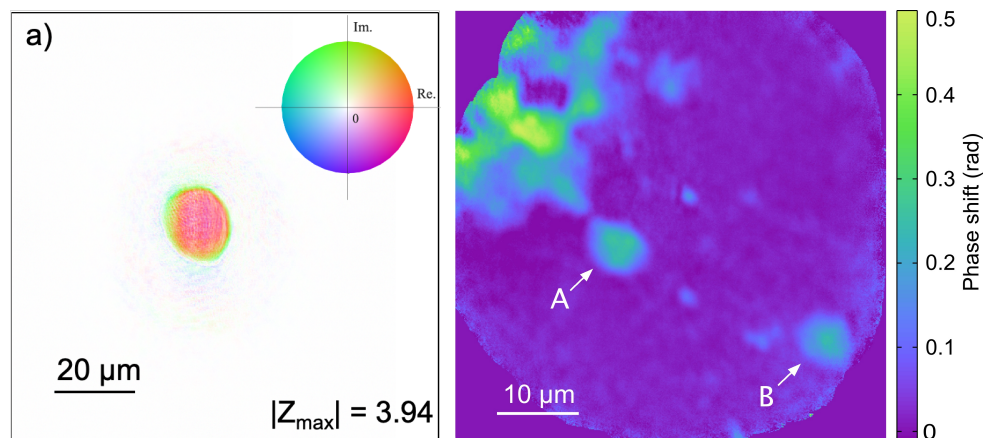


Figure 4. Reconstruction using virtual sub-pixels (2×2), a) probe function (HSV plot) and b) reconstructed phase shift.

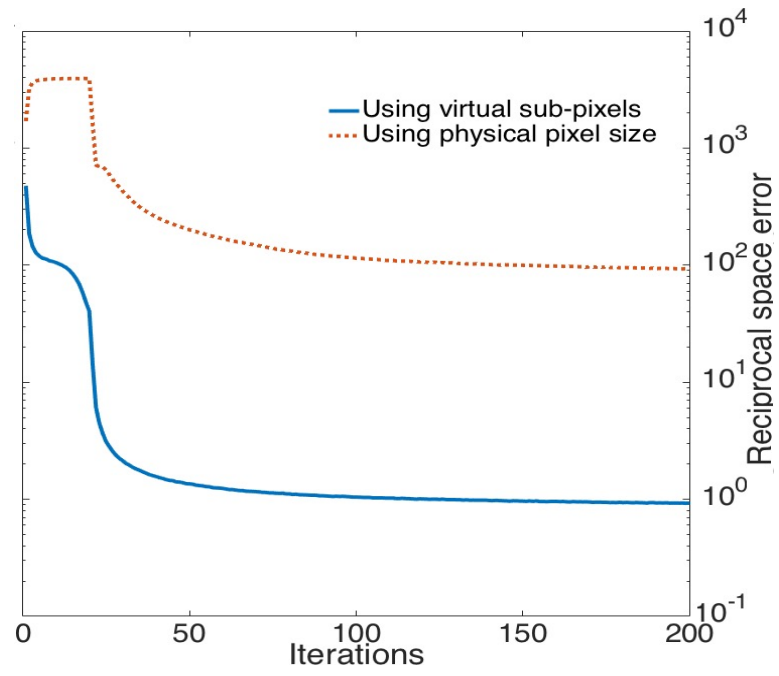


Figure 5. Comparison of the error function for phase retrieval with physical pixel size and with virtual sub-pixels (2×2).

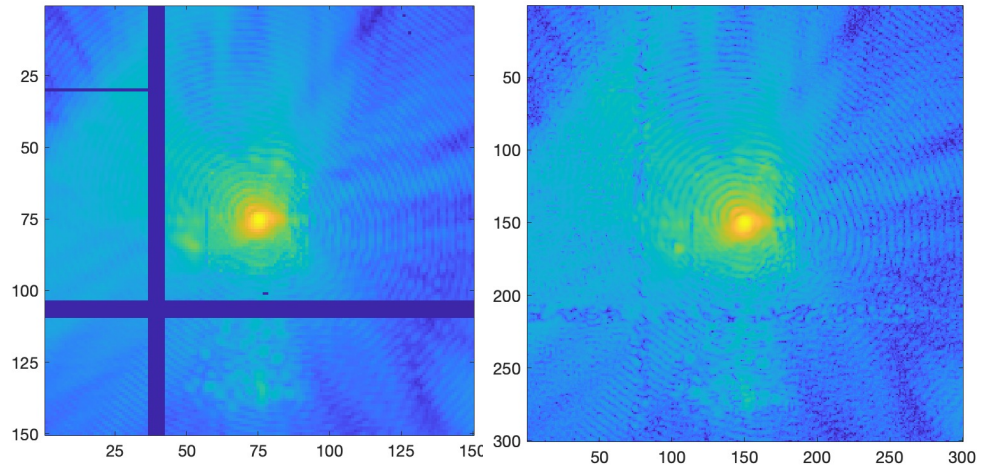


Figure 6: Comparison between the measured diffraction pattern (a), log plot) and the up-sampled iterated exit wave in the detector plane (b), log plot). The numbers represent pixels.

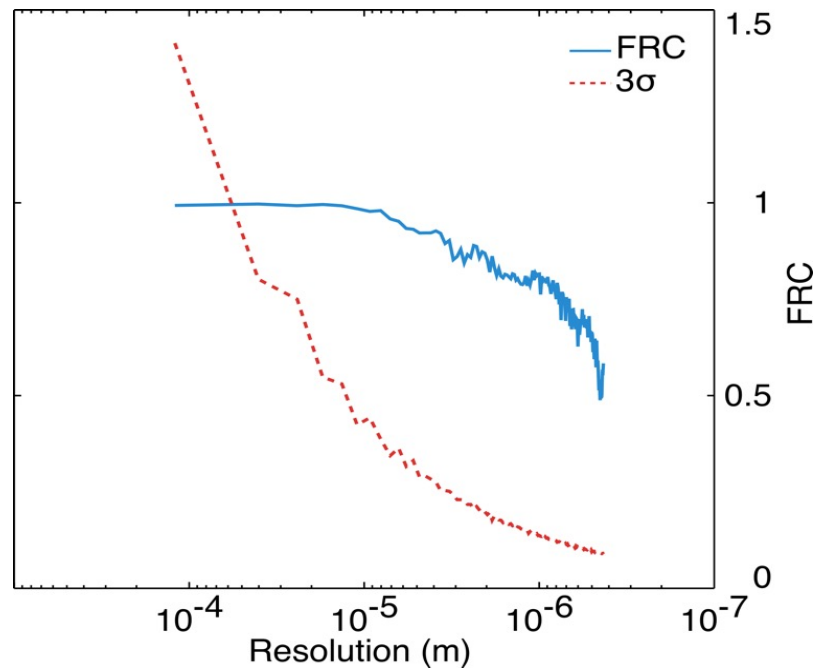


Figure 7. Fourier ring correlation of two separate and independent measurements of the same field-of-view. The red line shows the 3σ -noise level (Van Heel *et al.*, 2005).

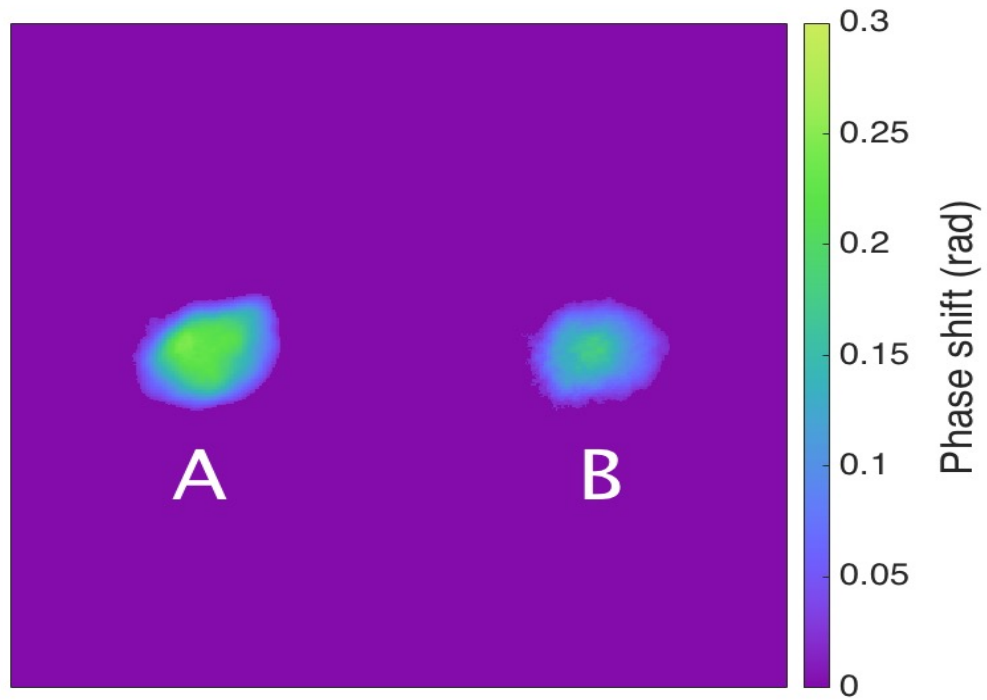


Figure 8. Isolated nuclei from the data shown in Fig. 2 a).

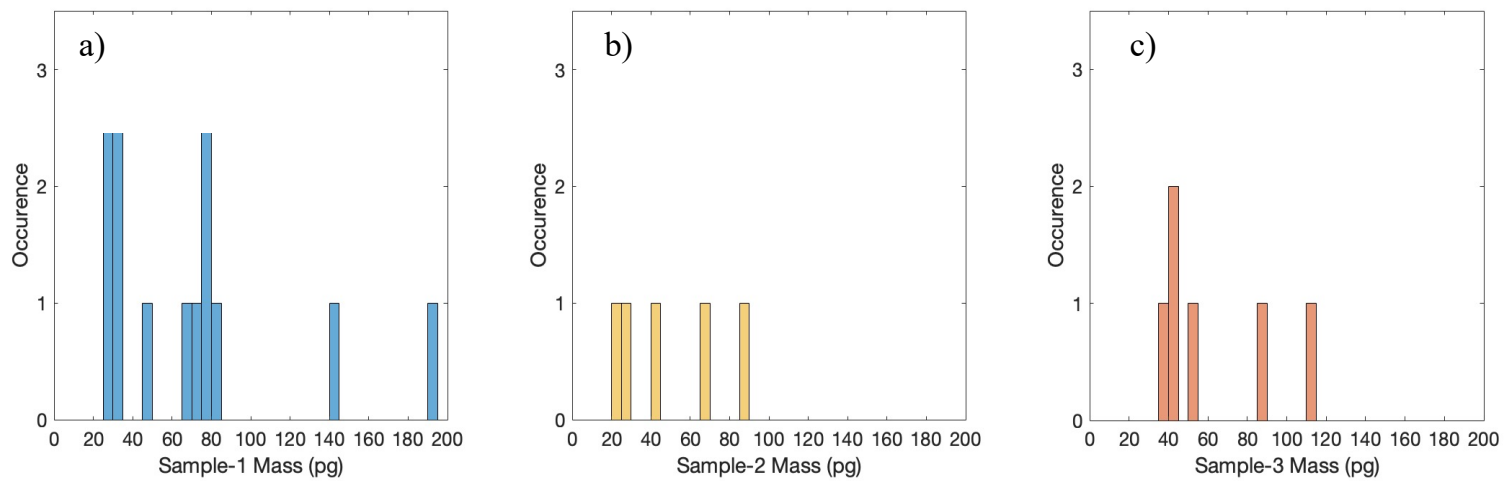


Figure 9. Histogram of observed nuclei mass. Sample-1 (stained) is shown in blue, Sample-2 (stained) is shown in yellow and Sample-3 (unstained) is shown in red. The height of the bars indicate the number of nuclei in a specific mass interval. Note that the three samples are shown separately and not as a sum.

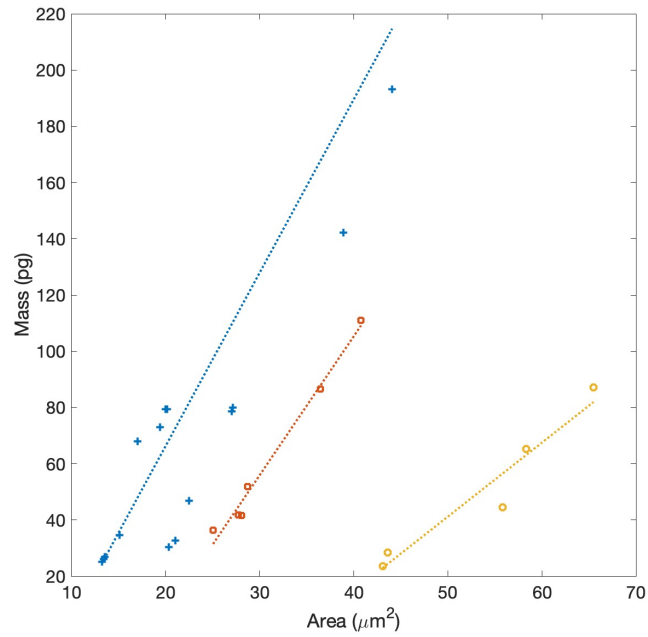


Figure 10. Observed nuclei mass against occupied area. Sample-1 (stained) is shown in blue, Sample-2 (stained) is shown in yellow, and Sample-3 (unstained) is shown in red.